JGR Planets

RESEARCH ARTICLE

10.1029/2025JE009582

Rocket Exhaust Derived Surface Water Migration at Lunar Landing Sites

Mingyu Tian[1], Yang Yang[2], Yuqi Qian[1,3], Ke Xu[2], Meizhu Wang[4], Lingzhi Sun[5], James Head[6], and Guochun Zhao[1]

[1]NWU-HKU Joint Center of Earth and Planetary Sciences, Department of Earth and Planetary Sciences, The University of Hong Kong, Hong Kong, China, [2]Department of Energy and Resources Engineering, College of Engineering, Peking University, Beijing, China, [3]Laboratory for Space Research, The University of Hong Kong, Hong Kong, China, [4]Key Laboratory of Space Active Opto-Electronics Technology, Shanghai Institute of Technical Physics, Chinese Academy of Sciences, Shanghai, China, [5]Hawai'i Institute of Geophysics and Planetology, University of Hawai'i at Mānoa, Honolulu, HI, USA, [6]Department of Earth, Environmental and Planetary Sciences, Brown University, Providence, RI, USA

Abstract Volatiles, especially water, are at the center of modern lunar explorations. They have various sources, including volcanism, asteroid/comet impacts, and Earth/solar wind implantations. However, due to the lack of in situ data, it has not been widely recognized that artificial activities, especially rocket exhaust, could significantly impact volatile behaviors on the Moon. Artificial impact becomes even more severe when the global community is marching toward the lunar south pole. Any artificially released volatiles could migrate to the cold traps in lunar polar regions, causing irreversible contamination for future explorations. The recent Chang'e-5 and 6 landers could conduct novel direct measurements of surface volatile migration, as they carried spectrometers covering water absorption wavelength, and landing cameras that can monitor rocket plume-regolith interactions. Based on their unprecedented data and quantitative water diffusion simulations, we propose an injection and release model of water on the lunar surface induced by rocket plumes. Our results depict the migration of lunar volatiles on the lunar surface on a fine scale, showing their resilience in a vacuum and hot environment by adhering to lunar soil regolith. We suggest that planetary protection must be considered for future explorations, especially those toward polar regions, from rocket exhaust until its effects can be mitigated.

Plain Language Summary In this work, we characterized lunar surface water migration behavior using spectral data and images collected by the Chang'e-5 and Chang'e-6 missions. The images clearly showed rocket plume-lunar regolith interactions. We proposed a comprehensive model for the water injection and release process on the lunar surface induced by rocket plumes. We found that rocket exhaust would inject water into lunar regolith and then gradually release it into space. According to our results, this process is slower than previously thought in a vacuum and hot environment, with water adhering to lunar soil grains. We also proposed that rocket exhaust could affect lunar surface water migration more effectively in cold places such as lunar polar regions.

Mingyu Tian and Yang Yang contributed equally to this work.

Key Points:

- We analyzed the variation of water content at Chang'e-5 and Chang'e-6 landing sites
- We estimated the plume-induced volatile behavior in lunar regoliths
- A numerical model was proposed to calculate the water release process

Supporting Information:

Supporting Information may be found in the online version of this article.

Correspondence to:

Y. Qian, K. Xu and G. Zhao,
yuqiqian@hku.hk;
kexu1989@pku.edu.cn;
gzhao@hku.hk

Citation:

Tian, M., Yang, Y., Qian, Y., Xu, K., Wang, M., Sun, L., et al. (2026). Rocket exhaust derived surface water migration at lunar landing sites. *Journal of Geophysical Research: Planets*, *131*, e2025JE009582. https://doi.org/10.1029/2025JE009582

Received 2 DEC 2025
Accepted 22 MAR 2026

1. Introduction

Volatiles on the Moon have long been a focal point of modern lunar exploration. Among different volatile species (H_2O, CO_2, S, Ar, He, etc.; Hurley et al., 2023), water/ice has captured major attention due to its scientific significance for understanding the hydration history of the inner Solar System, and as a potential resource for future in situ utilization (Chi Wang et al., 2024). Since the 1990s, different methods have been used to detect water/ice on the Moon and measure their contents from orbit (Colaprete et al., 2010; Fisher et al., 2017; Gladstone et al., 2012; Hayne et al., 2015; Honniball et al., 2020; S. Li et al., 2018; Milliken & Li, 2017; Pieters et al., 2009) and at the surface (H. Lin et al., 2022; Liu et al., 2022). Additional returned lunar sample analyses further supported the existence of water on the Moon in various forms and abundances (Anand et al., 2014; Chuanjiao Zhou et al., 2024; Jin et al., 2024; Saal et al., 2008).

On the basis of these lunar water detections, several key preliminary conclusions have been reached concerning their context, sources, spatial distribution, diurnal variation, etc. (Hurley et al., 2023; McCubbin et al., 2023). It is now well-recognized that major contributors to lunar volatiles include ancient lunar volcanism (Head et al., 2020), meteorite and comet impacts (Anand et al., 2014), and Earth and solar wind interactions with lunar regolith

(Chuanjiao Zhou et al., 2024). However, with advances in international lunar explorations, robotic and upcoming human activities on the Moon are bringing increasing quantities of volatiles to the Moon. The potential contamination caused by these activities cannot be ignored, especially when the lunar south pole has become a focal point of current lunar explorations (e.g., Chang'e-7/8, Artemis-3, LUPEX, and Luna-26 missions). For example, artificially released volatiles could migrate to the cold traps (Prem et al., 2025) in lunar polar regions, accumulate, and cause compositional contamination.

Among the range of robotic/human activities, engine exhaust plumes during the descent and landing process is a critical factor, since the engine plumes are close to the surface (Estacio et al., 2024), and fuel combustion process could create substantial volatiles ($4CH_3NHNH_2 + 5N_2O_4 = 9N_2 + 4CO_2 + 12H_2O$). In addition, the engine plumes are known to remove the top layer of regolith at landing regions (Clegg et al., 2014), creating the "blast zone" (BZ), which has been commonly observed at previous landing sites (Apollo missions, 23,800 m^2 in area; Luna missions, 2,400 m^2 in area; Chang'e-3 mission, 2,530 m^2 in area; and Chang'e-4 mission, 9,014 m^2 in area; Clegg-Watkins et al., 2016; Chao Wang et al., 2023; Y. Wang et al., 2023). Engine plumes have also been observed to erode lunar regolith vertically to a depth of a few centimeters based on high-resolution DEM images and mechanical simulations of the ejection of regolith particles by the engine plumes. For example, the average erosion depth of Chang'e-4 is ~0.7 cm (You et al., 2023), and the maximum erosion depth of Chang'e-5 reaches ~1.2 cm (~441 kg; You et al., 2023). The overpressure created by the engine could inject plumes into lunar regolith, causing interaction and erosion, and alter the chemical and physical properties of lunar regolith. For example, by removing the top mature regolith and lowering surficial submicroscopic metallic iron (SMFe) content, the rocket plumes affect the space weathering states of lunar regolith at previous landing sites (Clegg et al., 2014; Qian, Xiao, et al., 2024).

Examination of how engine exhaust plumes would affect lunar surface water contents became feasible only after the recent Chang'e-5 (CE-5) and Chang'e-6 (CE-6) missions of China's Lunar Exploration Program. The CE-5 mission landed in the northern part of Oceanus Procellarum in 2020 (Qian, Xiao, Wang, et al., 2021), and the CE-6 mission landed in the farside Apollo basin within the South Pole-Aitken basin in 2024 (Qian, Head, et al., 2024; Figures 1a, 1c and Figure S1 in Supporting Information S1). Both landers were equipped with a Landing Camera (LCAM) and a Lunar Mineralogical Spectrometer (LMS) (Changyi Zhou et al., 2022). This instrumentation allowed for the simultaneous characterization of plume release patterns and in situ surface water detection. The observation range of LMS covers an area of ~2 m^2 near the lander. The wavelength range of LMS is 480–3,200 nm, which includes the H_2O/OH absorption band at 2,850 nm (Xu et al., 2022). LCAM provides continuous images of the landing site during the entire descent process, acquired every single second.

To derive a more comprehensive understanding of lunar water behavior induced by artificial spacecraft activity, it is critical to evaluate exhaust plume-regolith interactions. This becomes even more important now, as an increasing number of missions are planned for the lunar south polar region, which is an area with extremely low surface temperatures (Gaddis et al., 2023). Obtaining such information would not only shed light on the interpretation of lunar volatile data of non-polar regions but also provide critical information that could assist the formulation of planetary protection protocols (Prem et al., 2025). In this study, we utilized scientific data collected by the recent CE-5 and CE-6 missions, international orbital observations (e.g., Lunar Reconnaissance Orbiter Narrow Angle Camera, Chandrayaan-1 Moon Mineralogy Mapper images, and Diviner temperature data), and the latest development of volatile diffusion models, to reconstruct the descent engine plume effects on lunar regolith. This study estimated the plume-induced volatile behavior in lunar regolith in order to gain a better understanding of water-regolith interactions to apply to future lunar exploration and volatile protection.

2. Materials and Methods

2.1. Lunar Mineralogical Spectrometer and In Situ Spectral Data Processing

LMS is one of the main payloads onboard both CE-5 and CE-6 landers. Its scientific scope is to detect mineral composition and the signal of H_2O/OH in the sampling areas, and compare with those measured in the samples. The wavelength range of LMS covers from 480 to 3,200 nm, including Visible and Near-Infrared band (VIS, 480–950 nm), Near-Infrared band (NIR, 900–1,450 nm), Short Wave Infrared band (1,400–2,300 nm), and Medium-Wave Infrared band (2,200–3,200 nm) (Xu et al., 2022).

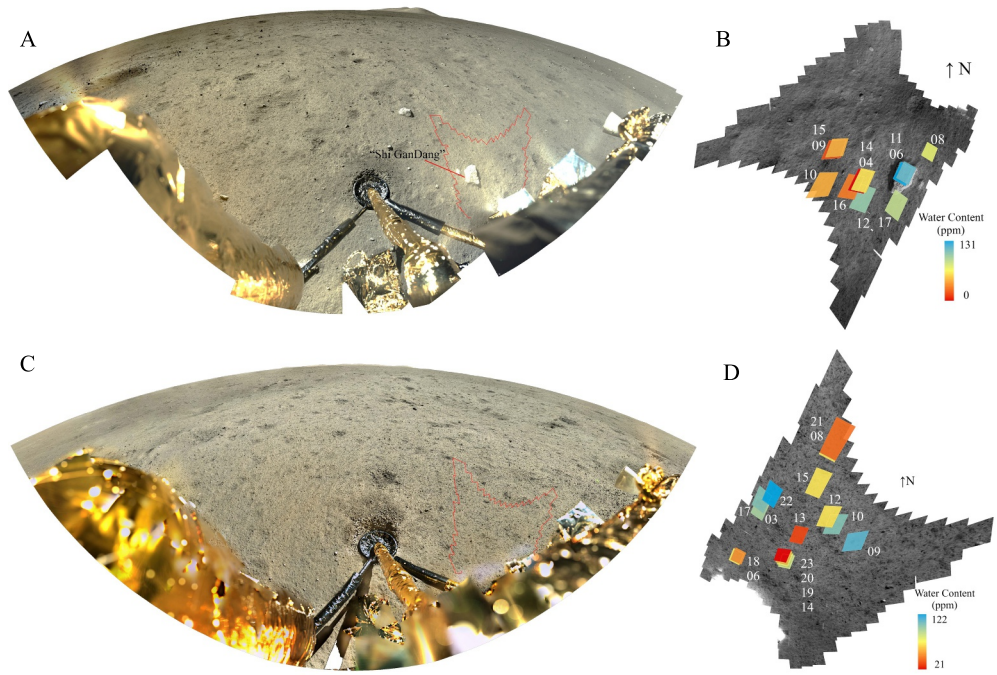

Figure 1. The observation regions of CE-5 (a) and CE-6 (b) LMSs. (a) The red line shows the full view of LMS. The base map is the image from the Panoramic Camera (PCAM) onboard CE-5 lander. (b) Detailed positions of the LMS 11 Full-Bands Observation detections. Detection 04 and 14, 09 and 15, 06 and 11 observed the same position at different times. The base map is composed of 180 images obtained from the LMS Full-View Scanning and Multispectral Observation detections. The water content values of each observed region are shown in different colors. (c, d) Similar to (a, b), but from CE-6 PCAM and LMS. Detection 06 and 18, 08 and 21, 14/19/20/23 observed the same position at different times. The water content values of each observed region are also shown in different colors.

To acquire the spectral information, LMS utilizes three operation modes. The first mode is the full-band observation (FBO) mode. It can acquire V-NIR spectral images as well as infrared spectral data at a sampling interval of 5 nm (588 bands). The second mode is the full-view scanning and multispectral observation (FVSMO) mode, which can acquire multispectral (20 bands) visible images and infrared data through 180 different detection targets. The third mode is the in-flight calibration (IFC) mode. This mode is used to acquire data in solar illumination from the calibration diffuser.

The LMS Level 2B radiance data were used in this study. These data have undergone several calibrations, including dark-current subtraction, scattering-background correction, flat field calibration, instrument temperature correction, radiometric calibration, and geometric calibration. The radiance factor (RADF) data of the lunar surface were first calculated using the solar irradiance (H. Lin et al., 2022):

$$\mathrm{RADF}(i,e,g) = \frac{I}{F}(i,e,g) = \frac{\pi I}{J/d^2} \tag{1}$$

In which I is the observed radiance, J is the solar irradiance at the top of the Earth's atmosphere, d is the distance between the Sun and the Moon (about 0.988 AU), i, e, and g are the incidence angle, emission angle, and phase angle, respectively.

Second, to obtain a continuous spectrum, data from the four bands were normalized to the NIR band, which served as the reference.

2.2. Thermal and Photometric Correction of LMS Data

Because the Moon is heated by solar irradiance, the thermal emission from the lunar surface can affect the observed spectral data. Based on the normal temperature of the lunar surface (50K–450K), its thermal emission mainly influences the wavelength after 2,000 nm. Therefore, the absorption features of H_2O/OH will also be

strongly affected or even obscured. The working time of LMS started at about 10 a.m. (lunar local time), so conducting thermal correction for the data is necessary.

The radiance observed by LMS before thermal correction can be expressed as

$$L = \frac{J}{\pi} * R + L_{bb}(T)(1 - R) \tag{2}$$

Where J is the solar irradiance (Gueymard, 2004), $L_{bb}(T)$ is the Planck function for a blackbody at temperature T, R is the real reflectance. Here we apply Kirchhoff's law, in which the emissivity $E = 1 - R$.

In this study, we used three thermal correction models. The first was Li's model (S. Li & Milliken, 2016). This model is based on the empirical relationship $R_{2540} = 1.124R_{1550}^{0.8793}$ of the reflectance at 1,550 nm and 2,540 nm. The reason for selecting these two wavelengths is that reflectance at 1,550 nm is not affected by thermal emission. On the contrary, reflectance at 2,540 nm is affected. The non-affected reflectance at 2,540 nm could be calculated using this relationship. Then, using the difference between the observed reflectance and calculated reflectance at 2,540 nm, the temperature could be calculated according to the Planck function. The second was Clark's model (Clark et al., 2011). Linear fitting of the reflectance at 1,700 nm and 2,350 nm was used in this model to predict the real reflectance at 3,100 nm. Then, the calculated real reflectance values at 2,280 nm and 2,600 nm were iteratively used. The temperature of each spectrum was derived when the difference between two iterations was less than 2K. The third model was Groussin's model (Groussin et al., 2007). In this model, the radiance was first normalized to 2,500 nm. Then, for different temperatures, the blackbody emission was computed based on the Planck function. Finally, the best fit temperature from 2,500 to 3,200 nm was derived by using a least-squares method.

LMS obtained data of different detection targets at different lunar local times. Therefore, the three observation angles (incidence angle, emission angle, and phase angle) varied significantly. To perform photometric correction, the Lommel-Seeliger model was used in this study, aiming to correct the data to standard view (incidence angle = 30°, emission angle = 0°, and phase angle = 30°). The model is expressed as follows:

$$f(g) = a_3 g^3 + a_2 g^2 + a_1 g + a_0 \tag{3}$$

$$\frac{I}{F}(30°, 0°, 30°) = \frac{I}{F}(i, e, g) \frac{\cos 30°/(\cos 30° + \cos 0°)}{\cos i/(\cos i + \cos e)} \frac{f(30°)}{f(g)} \tag{4}$$

The fitting coefficients are shown in Table S1 of Supporting Information S1, and the initial incidence/emission/phase angles are shown in Table 1. Those listed bands of the FBO data could be directly corrected using Equation 3, and the coefficients for other bands could be interpolated.

We mainly used the results calculated by Clark's method in the result and discussion sessions, since it would be more convenient to compare with the previous study (Liu et al., 2022) and the Level 2B M^3 data, which underwent Clark's thermal correction process. The original spectra and spectra after the above correction process are shown in Figure 2.

2.3. Water Content Estimation

The absorption features of water occur in several bands. The most obvious one is near 6 μm. However, this wavelength exceeds the detection range of LMS. The absorption features at 2,950 and 3,050 nm in the LMS data were too weak to analyze. Therefore, we used the absorption feature at 2,850 nm to represent the water content. The Single Scattering Albedo (SSA) was calculated based on the Hapke theory (Equation 5), and parameters can be referred to (S. Li & Li, 2011). The Savitzky-Golay algorithm was used to smooth the SSA values, and the Convex Hull method was used to remove the continuum. We then calculated the effective single-particle absorption thickness (ESPAT) values at 2,850 nm (Equation 6). The water content was calculated by an empirical formula (Equation 7) obtained from laboratory experiments (S. Li & Milliken, 2016). Results are shown in Figure 3.

Table 1
The Observation Time, Observation Angles (Incidence Angle, Emission Angle and Phase Angle) and Calculated Water Contents of CE-5 and CE-6 LMSs Data

		Observation angles (°)			Water content (ppm)		
ID	Local observation time	Incidence angle	Emission angle	Phase angle	Li's method	Clark's method	Groussin's method
CE5_D04	10:02	50.3	49.9	77.1	43	33	85
CE5_D06	10:05	50	44.4	81.8	109	114	114
CE5_D08	10:07	49.8	37.3	80.8	65	77	65
CE5_D09	10:07	49.7	48.7	66.2	3	16	6
CE5_D10	10:08	49.6	54.6	74.2	1	16	1
CE5_D11	10:08	49.5	44.4	81.7	120	131	126
CE5_D12	10:10	49.4	52.4	81.7	67	93	61
CE5_D14	10:20	48.3	49.9	78.7	0	1	0
CE5_D15	10:24	48	48.6	68.1	1	4	1
CE5_D16	10:32	47	51.7	80	2	8	2
CE5_D17	10:33	47	51.2	88.7	56	83	70
CE6_D03	09:57	51	48.4	93.8	83	59	53
CE6_D06	09:59	50.7	34.1	76.9	55	44	37
CE6_D08	10:00	50.6	63.2	112.5	79	44	14
CE6_D09	10:01	50.5	51.9	101.6	137	94	53
CE6_D10	10:02	50.5	51.7	102.1	112	74	37
CE6_D12	10:15	48.9	52.2	101	75	44	22
CE6_D13	10:16	48.7	44.8	93.4	27	23	24
CE6_D14	10:17	48.6	35.9	84.5	69	55	44
CE6_D15	10:19	48.4	56.6	104.7	56	44	1
CE6_D17	10:31	47.2	50.5	95.1	89	74	23
CE6_D18	10:32	47.2	34	76.3	41	36	27
CE6_D19	10:32	47.1	35.6	82.8	55	47	32
CE6_D20	11:00	44.9	35.7	80.2	45	37	34
CE6_D21	11:00	44.8	62.9	107.6	61	28	2
CE6_D22	11:01	44.8	51.9	96.3	155	114	1
CE6_D23	11:01	44.8	35.9	80.4	23	21	17

$$\frac{I}{F}=\frac{\omega}{4}\frac{\mu_0}{\mu_0+\mu}\left\{\left[1+B(g)\right]P(g)+H(\mu,\omega)\,H\left(\mu_0,\omega\right)-1\right\} \tag{5}$$

$$\mathrm{ESPAT}=\frac{1-\omega}{\omega} \tag{6}$$

$$\mathrm{H_2O(\,ppm)}=5900\times\mathrm{ESPAT} \tag{7}$$

For the M^3 data, we selected two 5 km × 5 km regions centered by the landing site of CE-5 and CE-6, then used the average spectrum of the regions to calculate the water content using the same method as described above, shown in Figures 4a and 4c; Figure S2 of Supporting Information S1. For CE-5, we found 3 M^3 images that cover the landing site, and for CE-6, we found 7 images.

2.4. Temperature Curve Fitting of Diviner Data

The Diviner Lunar Radiometer Experiment flew aboard the Lunar Reconnaissance Orbiter (LRO). Launched in 2009, it has been collecting solar reflectance and mid-infrared radiance measurements nearly continuously. The

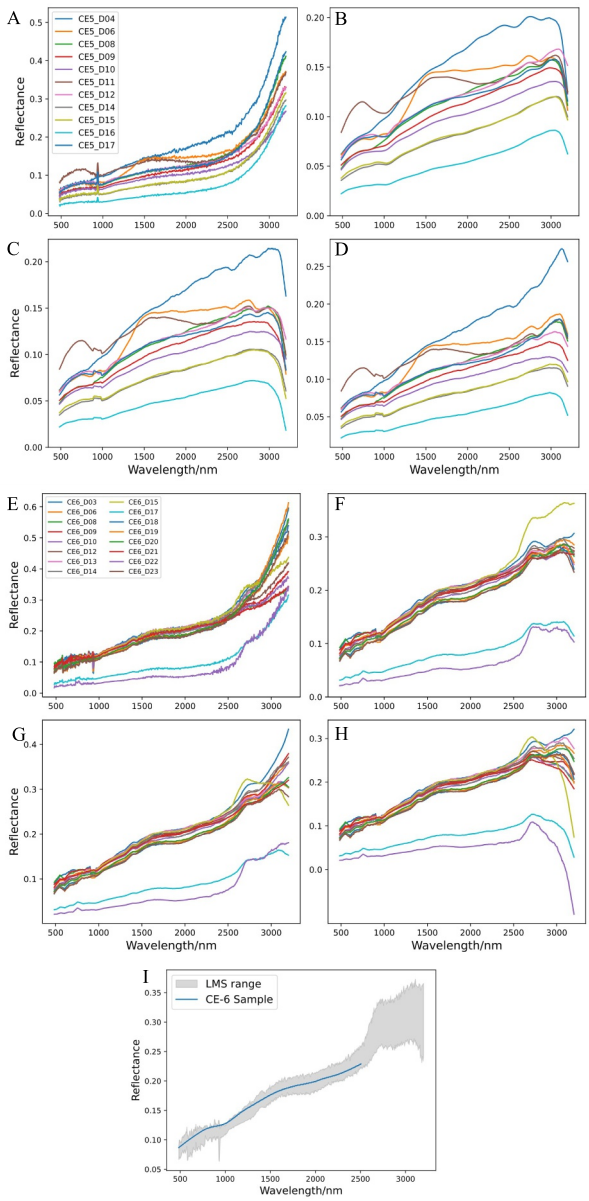

Figure 2. LMS Spectra data before and after thermal correction. (a) All the 11 FBO spectral data obtained by CE-5 LMS after radiometric correction. (B/C/D) Thermal correction result of CE-5 LMS data, smoothed by Savitzky-Golay algorithm. (b) Clark's method, (c). Li's method. (d) Groussin's method. (e) All the 16 FBO spectral data obtained by CE-6 LMS after radiometric correction. (F/G/H) Thermal correction result of CE-6 LMS data, smoothed by Savitzky-Golay algorithm. (f) Clark's method, (g) Li's method, (h) Groussin's method. (i) CE-6 sample spectra (X. Lu et al., 2025) compared with CE-6 LMS spectra.

Global Cumulative Products (GCP) acquired by Diviner contain the surface temperature of a $0.5° \times 0.5°$ region at different lunar local times. The temperature values of regions centered at $(-51.75°, 43.25°)$ and $(-154.25°, -41.75°)$ were selected because these regions contain the landing sites of CE-5 and CE-6. This data was downloaded from the PDS Geoscience Node.

Theoretically, the lunar surface temperature is mainly related to the surface emissivity E, absorptivity α, the area of the detected place A, and the total solar radiation L_{sun}. Applying Kirchhoff's law $E = 1 - R = \alpha$, this could be expressed as:

$$(1 - R)\sigma T^4 A = (1 - R) L_{\text{sun}} \tag{8}$$

For a relatively flat area, A is affected by the solar incidence angle i, therefore, the incident solar radiation could be expressed as

$$L_{\text{sun}} = \text{SAcos}(i) \tag{9}$$

Where S is the solar constant.

According to these two equations, we know that the surface temperature T is positively related to $\sqrt[4]{\cos(i)}$. The lunar local time could be calculated using the hour angle t as $\text{ltim} = (t + 180)/15$, and t could be calculated using spherical trigonometric function. The solar incidence angle i, the solar azimuth angle (a), the latitude (φ) of the detected area, and the R.A. of the sun (δ) would be used in the function:

$$\cos i = \sin\delta \sin\varphi + \cos\delta \cos\varphi \cos t \tag{10}$$

$$\sin\delta = \sin\varphi \cos i + \cos\varphi \cos i \cos a \tag{11}$$

Therefore, the lunar surface temperature T is also positively related to the lunar local time (Figures 4b and 4d). The temperature values were then fitted using $T = k_0\sqrt[4]{\cos(15 \times \text{ltim} - 180)}$, where k_0 is the coefficient to be determined (Ren et al., 2024).

2.5. LROC NAC, Chang'e-5 and Chang'e-6 LCAM Data Processing

Lunar Reconnaissance Orbiter Camera (LROC) consists of two Narrow Angle Cameras (NACs) and one multispectral Wide Angle Camera (WAC). The mission (LRO) was launched in 2009. NACs are monochrome push-broom scanners (Robinson et al., 2010). The resolution of NAC images could reach 0.5 m/pixel. WAC data provide a global image of the lunar surface with a resolution of 100 m, and were used for calibration in this study. The product IDs of NAC images taken before and after the landing of CE-5 are M1348581418LE and M1361560086LE, respectively. Similarly, the product ID of the NAC image taken before the landing of CE-6 was M1305784636LE, and the one taken after the landing of CE-6 was M1472410644LE. Figure 5 shows the selected NAC images. The NAC images were downloaded from the PDS Geoscience Node and calibrated using the Integrated Software for Imagers and Spectrometers (ISIS3, https://isis.astrogeology.usgs.gov/8.1.0/Installation/index.html) version 3 for georeferencing to the LROC WAC global mosaic.

The landing camera (LCAM) is a scientific payload that captures images of the lunar surface during the descent process to assist obstacle avoidance. Two LCAMs were set at the bottom of the CE-5 and CE-6 landers. In this

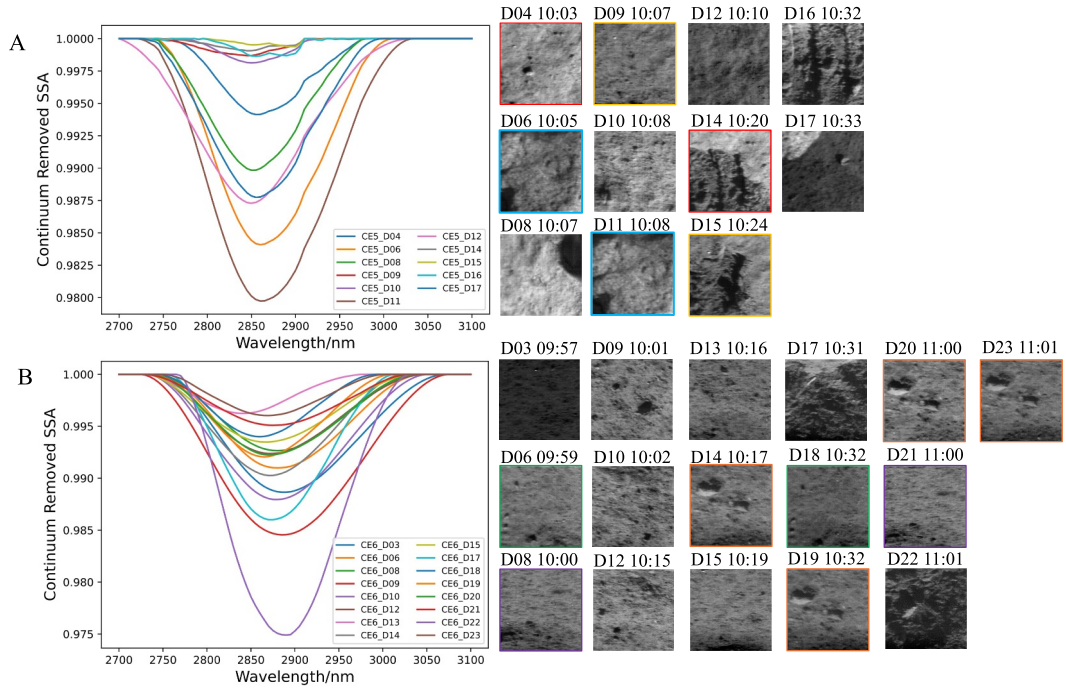

Figure 3. Continuum removed absorption features and detailed images. The 2,700–3,100 nm continuum removed the absorption features of the LMS FBO hyper-spectra and detailed images of FBO detections for CE-5 (a) and CE-6 (b). Each group of spectra that detected the same place was marked with the same color frame.

study, the Level 2B data of LCAM were used, as shown in Figure 5. The images were then georeferenced to the above NAC images.

2.6. Quantitative Model of Water Interaction With Lunar Regolith

Due to the high vacuum environment, the mean free path of water molecules in the regolith is comparable to or larger than the lunar regolith particle size. As a result, vapor molecules diffuse mainly in the Knudsen diffusion mode (Gunn & King, 1969). Meanwhile, water molecules may adsorb on the regolith particle surface. Governing equations of vapor and heat transfer in the regolith are:

$$\frac{\partial(\phi C + C_a)}{\partial \tau} + \nabla \cdot (-D_{\text{eff}} \nabla C) = 0 \tag{12}$$

$$\rho_r C_{p,r} \frac{\partial T}{\partial \tau} + \nabla \cdot (-k \nabla T) = 0 \tag{13}$$

where ϕ denotes porosity, C denotes water vapor concentration, C_a denotes adsorbed water abundance, τ is time, D_{eff} is the effective diffusion coefficient, ρ_r is the bulk density of Lunar regolith, $C_{p,r}$ denotes regolith specific heat, k is the thermal conductivity. Effective diffusion coefficient D_{eff} is determined as: (He et al., 2014)

$$D_{\text{eff}} = \frac{D_{O,\text{eff}} \cdot D_{Kn,\text{eff}}}{D_{O,\text{eff}} + D_{Kn,\text{eff}}} \tag{14}$$

where $D_{Kn,\text{eff}} = \frac{d_v v}{3} \cdot \frac{\phi}{\xi}$ and $D_{O,\text{eff}} = \frac{\lambda_m v}{3} \cdot \frac{\phi}{\xi}$ are effective Kundsen diffusion coefficient and ordinary diffusion coefficient (Reinecke & Sleep, 2002), respectively. Here, d_v is the pore size, λ_m is the mean free path of water molecules in open space, v is the speed of the molecule, and ξ is the tortuosity of porous regolith. Adsorbed water abundance C_a is determined by assuming local equilibrium and adopting Langmuir adsorption theory (Swenson & Stadie, 2019):

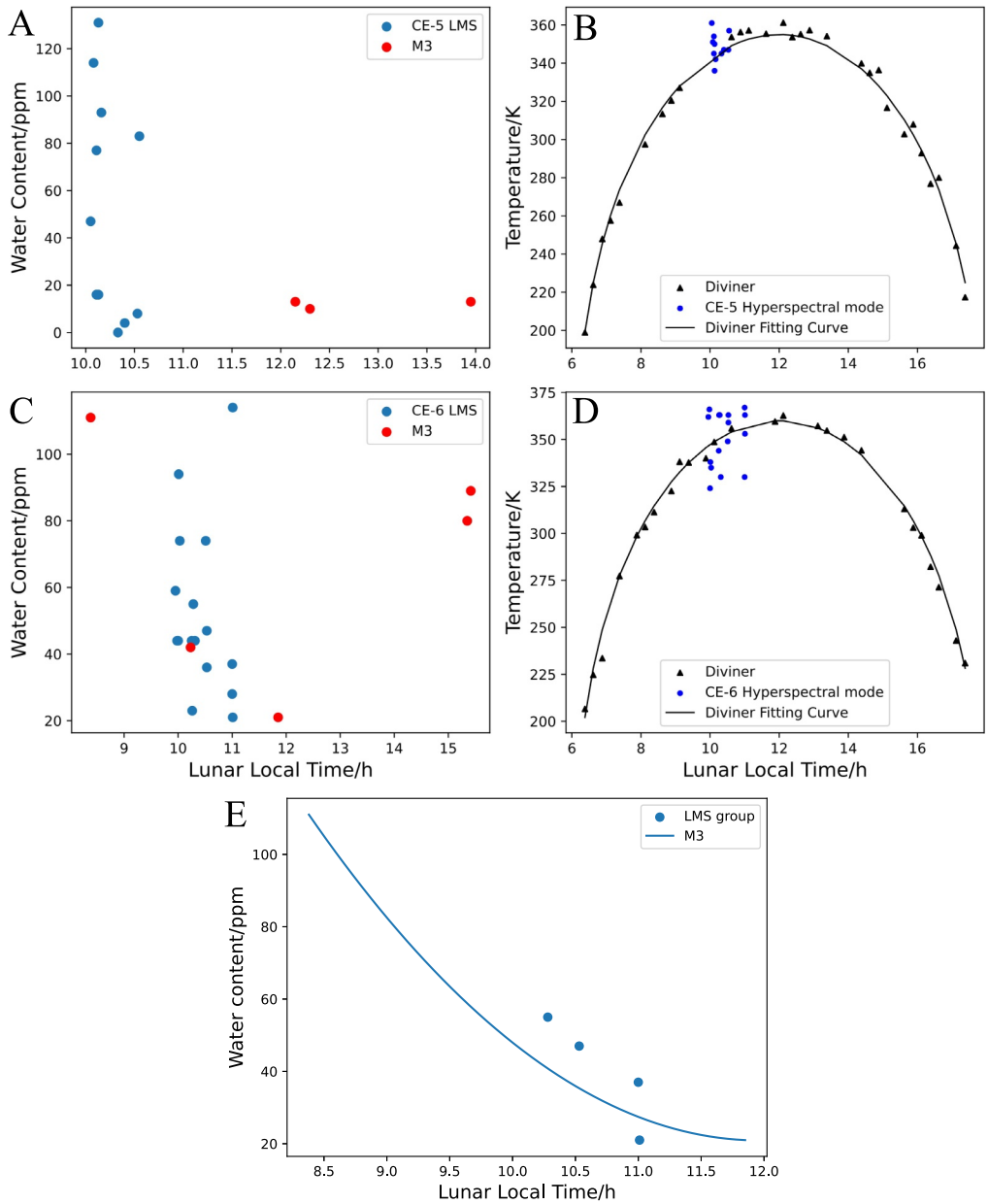

Figure 4. The calculated water content of CE-5 and CE-6 LMSs compared with M^3 data, and the calculated surface temperature of LMS data compared with Diviner data. (a) Water content of CE-5 LMS 11 FBO data (blue dots) and water content of 3 M^3 data covered CE-5 landing site (red dots). (b) The calculated lunar surface temperature of CE-5 LMS 11 FBO data (blue dots) and Diviner GCP data (black triangles). (c) Water content of CE-6 LMS 16 FBO data (blue dots) and water content of 7 M^3 data covered the CE-6 landing site (red dots). (d) The calculated lunar surface temperature of CE-6 LMS 16 FBO data (blue dots) and Diviner GCP data (black triangles). (e) Water content of spectra number 14, 19, 20, and 23 (blue dots) compared with quadratically fitted M^3 data (before noon).

$$C_a = \frac{C_m \cdot \mathrm{KP}}{1 + \mathrm{KP}} \tag{15}$$

where $C_m = \mathrm{SSA} \cdot \rho_r \cdot A_m$ denotes water abundance corresponding to complete monolayer coverage, SSA is the specific surface area that equals to the total area of particles over its' total mass, A_m is the amount of water molecules per square meter, $P = CR_gT$ is pressure, R_g is the universal gas constant. The adsorption equilibrium

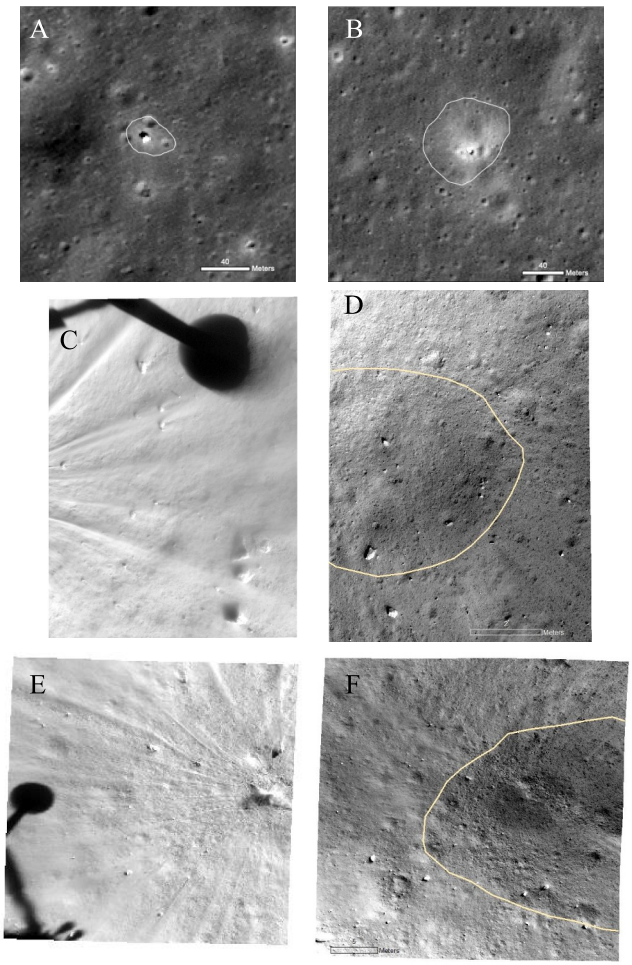

Figure 5. Blast zones at CE-5 and CE-6 landing sites. HR-BZs (white lines): (a) CE-5 landing site, background figure M1361560086LE; (b) CE-6 landing site, background figure M1472410644LE. LR-BZs (stripes and orange lines): (c) The plume shown on CE-5 LCAM image (LCAM-1-0416_SCI_N_20201201151110_20201201151110_0001). (d) The low reflectance blast zone of CE-5 (LCAM-1-0413_SCI_N_20201201151106_20201201151106_0001). (e) The plume shown on CE-6 LCAM image (LCAM-1-0425_SCI_N_20240601222306_20240601222306_0001). (f) The low reflectance blast zone of CE-6 (LCAM-1-0423_SCI_N_20240601222305_20240601222305_0001).

coefficient K, which represents the ratio of adsorption rate to desorption rate at equilibrium, is calculated as: (Swenson & Stadie, 2019)

$$K = \frac{\frac{1}{\sqrt{2\pi MRT}}}{\nu \cdot e^{\left(\frac{E_{de}}{k_B T}\right)} \cdot A_m} \tag{16}$$

where E_{de} is the adsorption energy, k_B is the Boltzmann constant, ν is the frequency factor, M is the molecular mass of water.

To compare our quantifications to the effective water content detected by LMS and M^3 infrared spectroscopy, we need to estimate the detection penetration depth (the depth where radiation is reduced to $1/e$ of its original value) corresponding to the characteristic absorption wavelength of water (2,850 nm) using Equation 17 (Chuanjiao Zhou et al., 2022; Lv et al., 2018):

$$D_{\text{penetration}} = \frac{\lambda_w}{2\pi} \cdot \frac{\sqrt{\varepsilon'}}{\varepsilon''} \tag{17}$$

where λ_w denotes wavelength, ε' and ε'' denote the real part and imaginary part of the dielectric constant, respectively. The mean dielectric permittivity of lunar regolith is estimated to be 2.96 + 0.03i, which is derived from its composition and porosity (Jia et al., 2021). Based on the estimated penetration depth, we determined the linear attenuation coefficient μ_a in the Lambert-Beer law. Using this coefficient, we then performed a weighted average of the adsorption capacity profile according to Equation 18, thereby estimating the effective surface water content (Lv et al., 2018) $C_{a,\text{eff}}$ corresponding to LMS or M^3 infrared spectral detection by Equation 19. Equations are:

$$I_L = I_{L,0} \cdot e^{-\mu_a x} \tag{18}$$

$$C_{a,\text{eff}} = \frac{\int_0^{L_c} C_a(x) \cdot e^{-\mu_a x} dx}{\int_0^{L} e^{-\mu_a x} dx} \tag{19}$$

where x is depth, $I_{L,0}$ and I_L are the light intensity before and after penetration, respectively, L_c is the length of the one-dimensional computational domain, $C_a(x)$ is the adsorption capacity corresponding to depth x.

The selection of parameters and boundary conditions in the calculation is shown in Table 2. The initial conditions for heat and mass transfer were derived from the M^3 water content data. Since there are no thermal conductivity data for the lunar soil from CE-6, we referred to the thermal conductivity range of the lunar soil measured by CE-4 from the South Pole-Aitken basin like CE-6 (Xiao et al., 2022; Zheng et al., 2023).

2.7. Constraining Model Parameters Based on Remote Sensing Observations

To ensure the physical correctness of our interpretive calculations for the LMS data, determining the initial and boundary conditions for temperature and water vapor concentration is essential. This is achieved by utilizing the only two available data sets: Diviner temperature measurements and M^3 water content data.

For each selected combination of adsorption energy and pore size, two unknown parameters are required to fit the M^3 data: the intrinsic water vapor concentration (serving as the mass transfer boundary condition at the lunar surface) and the intrinsic hydroxyl content. The total water content used for comparison with M^3 data is the sum of adsorbed water (calculated from the model) and the intrinsic hydroxyl content, as the M^3 and LMS measurements both reflect water content converted from hydroxyl.

Journal of Geophysical Research: Planets

10.1029/2025JE009582

Table 2
Parameter Settings and Boundary Conditions

Parameters	Units	Values	Description	References/Sources
Basic parameters				
d_p	μm	5.41–38.98	Mean size of 95% CE6 particles (5.41)—Mean size of 95% mass of CE6 particles (38.98)	C. Li et al. (2024)
ρ_r	kg/m^3	983	Bulk density of CE6 lunar regolith	
ρ_p	kg/m^3	3035	Particle density of CE6 regolith	
ϕ	1	$0.676 = 1 - \frac{\rho_r}{\rho_p}$	Porosity of regolith	/
τ	1	$1.216 = \phi^{-1/2}$	Tortuosity of regolith	Tjaden et al. (2016)
$d_{p,\mathrm{CE5}}$	μm	3.96	Mean size of 95% CE5 particles (in number)	C. Li et al. (2022)
$\mathrm{SSA_{CE5}}$	m^2/kg	560	Mean diameter of CE5 regolith particles	
SSA	m^2/kg	$410 = \mathrm{SSA_{CE5}} \times \frac{d_{p,\mathrm{CE5}}}{\min(d_p)}$	Specific surface area of CE6 regolith.	/
ν	s^{-1}	1×10^{13}	Frequency factor	Clendenen et al. (2022), Jones et al. (2020), Poston et al. (2015), Schörghofer (2023)
E_{de}	eV	0.6–1.6	The range of adsorption energy of lunar regolith	
k	W/(m·K)	2.3×10^{-3}	Typical thermal conductivity of lunar regolith	Keihm (1984), Xiao et al. (2022), Zheng et al. (2023)
$C_{p,r}$	J/(kg·K)	$593.13 = 670 + 10^3\left(\frac{204.87-250}{530.6}\right) + 10^3\left(\frac{204.87-250}{498.7}\right)^2$	Typical specific heat of lunar regolith	
Boundary conditions				
T_{surface}	K	96.79–362.76	Surface temperature of CE6 landing-site	Diviner Global Cumulative Product
T_{bottom}	K	204.87	Time-averaged surface temperature of CE6 landing-site	Time average of T_{surface}
$T_{\mathrm{surface,CE7}}$	K	40.35–216.42	Surface temperature of CE7 landing-site	Diviner Global Cumulative Product
$T_{\mathrm{bottom,CE7}}$	K	98.45	Time-averaged surface temperature of CE7 landing-site	Time average of $T_{\mathrm{surface,CE7}}$
C_{surface}	mol/m^3	From the fitting calculations of M^3 data	Water vapor concentration at lunar surface from fitting	See Section 2 for details
C_{bottom}	mol/m^3	No flux	Bottom boundary condition	/

Note. SSA conversion note: Direct CE-6 specific surface area measurements are not yet available; therefore, CE-6 SSA is estimated by scaling the CE-5 SSA with the ratio of representative particle size (SSA_CE6 = SSA_CE5 x d_p,CE5/min(d_p)). k and C_{p,r} note: Because in situ CE-6 thermophysical measurements are currently unavailable, representative lunar-regolith values from CE-4/Apollo-based literature were adopted for k and C_{p,r} within physically reasonable ranges. These parameters mainly affect the thermal timescale and do not change the qualitative conclusion that plume-injected water can persist in shallow regolith over the observed period. A sensitivity check using plausible k and C_{p,r} values yielded the same first-order decay behavior and parameter regime for the best-fit case.

The fitting procedures are

1. For a given adsorption energy and pore size, an initial guess is made for the intrinsic water vapor concentration to serve as the surface boundary condition. The initial conditions assume no water vapor or adsorbed water inside the regolith.
2. Using the Diviner temperature data as the time-dependent surface temperature boundary condition, a 5-day heat transfer simulation is run to establish a stable initial temperature profile for the M^3 fitting simulation.
3. Coupled heat and mass transfer calculations are then performed. The mass transfer calculation uses the initial and boundary conditions together with the computed temperature distributions to solve for the water vapor and adsorbed water distributions over time.
4. The calculated profile of adsorbed water is added to a guessed intrinsic hydroxyl content to produce a total water content curve. The Mean Squared Error (MSE) between this curve and the M^3 data points is computed.
5. An optimization process iterates different combinations of intrinsic water vapor concentration and intrinsic hydroxyl content until the MSE is minimized.

Upon completion of this fitting process for a given parameter set, the resulting profiles are used for LMS data interpretation:

1. The temperature and concentration profiles from 09:15 on the sixth simulated day were used as the initial conditions for Stage 1 of the LMS interpretive calculation.
2. The optimized intrinsic water vapor concentration is used as the mass transfer boundary condition for Stage 2.
3. The optimized intrinsic hydroxyl content is added to the adsorbed water calculated in the LMS simulation stage to generate a total water content curve for direct comparison with the LMS data points.

Results are shown in Figure S3 of Supporting Information S1. During our analysis, we identified that the adsorption energy range needed refinement. The initial range of 0.6–1.2 eV, based on Apollo samples, led to unphysical results at the lower end (e.g., an adsorption energy of 0.6 eV required an implausibly high intrinsic water vapor concentration of $\sim 10^{-4}$ mol/m^3) that contradicted the M^3 data. This concentration exceeds the upper limit of the lunar atmospheric pressure range (10^{-10}–10^{-8} Pa) reported in literature (Schörghofer, 2023). To account for potential measurement uncertainties, we conservatively extended this range by one order of magnitude at both ends (10^{-11}–10^{-7} Pa) for our constraint. Compared with the initial Apollo-informed adsorption-energy prior, the CE-5/CE-6-constrained range is notably narrower, indicating that the local regolith-water interaction is better represented by moderate-to-strong binding in our model framework. Because molecular residence time depends exponentially on adsorption energy, even a modest narrowing of the energy range substantially reduces uncertainty in predicted volatile persistence. This helps explain why plume-emplaced water can remain detectable in shallow regolith for several lunar hours after landing. At the same time, adsorption energy and effective pore size are not fully independent in inversion, and therefore, the constrained range reported here should be interpreted as an effective range conditioned on current boundary conditions and data sets. By applying this constrained pressure range and an MSE threshold of 500, we determined that adsorption energies below 0.9 eV yield poor fits. Consequently, the inversion calculations were performed within the narrowed range of 0.9–1.2 eV.

2.8. Sensitivity Analysis for Plume Pressure and Duration

We used the control variable method to study the effects of different plume pressures and plume durations on the calculation results. We plotted the normalized average water content at a depth of 30 μm in the surface layer immediately after the plume ended for different cases in Figure S4 of Supporting Information S1. As shown in Figure S4 of Supporting Information S1 (pore size of 20 μm), as long as the adsorption energy is higher than 0.8 eV (covering the range of adsorption energies that can fit the LMS data well), when the plume pressure is greater than 5 Pa or the plume duration is longer than 1s, the impact of the plume on our calculations is extremely limited. Therefore, we consider the possible pressure of 20 Pa and duration of 10 s in the actual landing process as the plume setting conditions in our other calculations.

3. Results

3.1. CE-5 and CE-6 In Situ Measurements of Water Contents

On the basis of the LMS data, the water content values ranged from ∼0 to ∼131 ppm at the CE-5 landing site (Figure 1b), with an average value of 52.4 ppm. The highest value, 131 ppm, was obtained from CE5-D11, whose target was a rock named "Shi Gandang" (Figure 1a), a porous fresh basalt about 1 m from the lander. As for the CE-6 LMS detections, the water content values ranged from ∼20 to ∼114 ppm (Figure 1d), with an average value of 42.2 ppm, ∼10 ppm lower than the CE-5 LMS results (Table 1). The highest value was from CE6-D22 (114 ppm), with relatively low reflectance and large shadows (Figure 3b). Compared with previous studies of CE-5 LMS (H. Lin et al., 2022; Liu et al., 2022), the water content detected by CE5-D11 (Figure 3a) was the highest among all studies and could reach ∼180 ppm (H. Lin et al., 2022). As for the lunar regolith, the water content varied from ∼2 to ∼110 ppm (H. Lin et al., 2022; Liu et al., 2022). Most observations of the lunar regolith (e.g., CE5-D09, D14, D15) showed very low water content (<15 ppm) in all three studies.

Duplicate or multiple LMS observations were made at six locations that enabled the analysis of water content variation at the CE-5 and CE-6 sites over time, as shown in Figure 4. For CE-5, there were three groups of spectra observed at the same locations, including CE5-D04/D14 (Group 1, 10:03/10:20, lunar local time, hereinafter), CE5-D06/D11 (Group 2, 10:05/10:08), CE5-D09/D15 (Group 3, 10:07/10:24). There were three spectra groups that observed the same locations by the CE-6 LMS, that is, CE6-D06/D18 (Group 4, 09:59/10:32), CE6-D08/D21 (Group 5, 10:00/11:00), and CE6-D14/D19/D20/D23 (Group 6, 10:17/10:32/11:00/11:01). Their water contents are all shown in Table 1 and will be discussed in detail in the following section. In addition, we used M^3 orbital hyperspectral data acquired over the CE-5 and CE-6 landing sites. This allowed us to compare the water absorption feature at ∼2,850 nm across broader spatial and temporal scales after quadratic fitting (Figure 4e). The CE-5 landing site was covered by 3 strips of M^3 images, collected at local times of 12:09, 12:18, 13:57, respectively. 6 strips of M^3 images that cover the CE-6 landing site, which were measured at local times of 08:23, 10:06, 10:14, 11:51, 15:21, 15:25, respectively (Figure S2 in Supporting Information S1). The water content values derived from M^3 data showed a clear trend with lunar local time. It decreased before noon and increased afterward.

3.2. Rocket Exhaust at the CE-5 and CE-6 Landing Sites

Rocket plume-lunar regolith interactions are readily observed at all lunar landing sites (Clegg et al., 2014), including the CE-5 (Qiao et al., 2023) and CE-6 landing sites investigated in this study. Images obtained by the LRO NAC before and after the landing of CE-5 and CE-6 and LCAM data were used to evaluate the rocket plume-lunar regolith interactions during the landing process (Figure 5). For CE-5, a BZ of ∼890 m^2 was identified (NAC image M1361560086LE, Figure 5a) in an elliptical shape. The average reflectance value in this region was ∼17.8% higher than that of the surrounding region. For the CE-6 landing site, the identified BZ (NAC image M1472410644LE) was about 4,800 m^2 (Figure 5b) in a relatively round shape. This was about 5.4 times larger than that of CE-5, which was likely due to topographic effects on plume flows (CE-6 landed on the rim of an impact crater) or due to additional rocket plume released. The average reflectance value in the CE-6 BZ was ∼20.9% higher than that of the surrounding region. In addition, a clear radial pattern caused by the engine plume was distinguished on the LCAM images for both CE-5 and CE-6 missions (Figures 5c and 5e).

Rocket exhaust typically creates a low-reflectance blast zone (LR-BZ) several meters in diameter at the center of the impact area, without removing the underlying mature regolith, due to flow stagnation (Zhang et al., 2022). These LR-BZs were also identified in the CE-5 and CE-6 LCAM images (Figures 5d and 5f), but their diameters decreased when the landers approached the lunar surface. LR-BZs are completely beneath the landers when CE-5 and CE-6 touched down on the surface, and thus are not observable from post-landing LRO NAC images.

Evidence from both NAC and LCAM images indicates that prominent rocket exhaust effects occurred at the CE-5 and CE-6 landing sites, which could have significant effects on regolith properties.

4. Discussion

4.1. Variations of Water Contents at the Chang'e-5 and Chang'e-6 Landing Sites

The water contents were calculated after conducting three different kinds of thermal corrections. The three groups of values differed slightly from each other. Groussin's model only considered fitting the temperature effect and ignored the spectrum itself, which led to unstable results. Therefore, we suggest that this model might not be the most suitable one. Li's model and Clark's model were both rigorous, and their results showed similar descending trends toward the lunar local noon. Compared with Li's model, Clark's model utilized a wider wavelength range and could be easier to compare with the M^3 data. Therefore, we mainly used Clark's method for further analysis.

Variations of water content at the CE-5 and CE-6 landing sites were observed in this study (Figures 4a and 4c and Table 1). Several key factors might account for the spatial and temporal variations of the measured water contents, including (a) diurnal change of surface temperature, (b) solar wind intensity, and (c) rocket plume and surface interactions. We assess all these factors in this and the subsequent sections.

The water contents of lunar regolith for Groups 1, 3, 4, 5, and 6 show clear decreasing trends toward noon, similar to previous orbital observations (Y. Lu et al., 2024) but constrained from the surface. For CE-5, the water content decreased from ∼47 to almost ∼0 ppm (Group 1) and from ∼14 to ∼6 ppm (Group 3). For CE-6, the water contents decreased from ∼44 to ∼36 ppm (Group 4) and from ∼44 to ∼28 ppm (Group 5), respectively. Multiple observations of CE-6 Group 6 (CE6-D14/D19/D20/D23) also supported this trend, which decreased from ∼55 to ∼21 ppm. The most probable factor controlling this remarkable decrease is the increase in surface temperature toward noon (Y. Lu et al., 2024). Therefore, we analyzed the surface temperatures using LMS spectra and the Diviner Global Cumulative Products (GCP) data (Williams et al., 2017) to evaluate and constrain the temperature impacts on water behaviors at both landing sites. During the thermal modeling of LMS, the temperature of each spectrum could be constrained, and this temperature is regarded as the surface temperature of the investigation areas (see Section 2.2). The GCP data was used to provide a reference value, fitted using the curve $\mathbf{T = k_0\sqrt[4]{\cos(15 \times ltim - 180)}}$ (see Section 2.3). Temperature values calculated using the two data sets are shown in Figures 4b and 4d. The temperature variation calculated by the LMS spectrum was relatively high while the GCP data showed a relatively smooth curve, perhaps attributable to resolution differences. Here, we only use GCP data as a reference. The total observation process of CE-5 LMS lasted about half an hour (lunar local time), and for CE-6, the process was about 1 hr. Based on Diviner data, the surface temperature at CE-5 and CE-6 landing sites rose about 5K and 10K during the observation process toward noon, accelerating the water loss rate of the entire landing site (Figure 4).

Solar wind implantation (H^+) is another major generator for lunar surface water. An increase in solar wind intensity could increase the lunar surface water content by reacting with silicate minerals (Chuanjiao Zhou et al., 2024; Jones et al., 2018). The farside CE-6 landing site would be exposed to the Sun when the Moon is between the Earth and the Sun, and when the Moon orbits to the far side from the Sun, the nearside CE-5 landing site would face the Sun but would be shielded by the Earth's magnetic field (J. Lin et al., 2025). Integrating all these effects, the solar wind intensity at CE-6 landing site, which is located on the lunar farside, is predicted to be nearly 50% higher than that at the CE-5 nearside landing site (J. Lin et al., 2025). Therefore, the solar wind derived water content at the CE-6 landing site should be higher than that at the CE-5 landing site. Our result showed that the lowest water content value at the CE-6 site (∼21 ppm) was indeed higher than CE-5 (∼0 ppm). This may explain the reason that, despite a decrease in water content for both missions after landing, the water content at the end of each group's observation was higher at the CE-6 landing site (>20 ppm) compared to CE-5 (∼1 ppm). This difference was observed even though the surface temperature at the CE-6 site reached a higher value (∼360K). In addition, since the solar wind intensity significantly decreases with depth (Kulchitsky et al., 2018), the water content produced tends to decrease. The duplicate LMS observations before and after the scoop sampling operations (Figures 1b and 1d) could test this. The water contents derived from spectra CE5-D04 and CE5-D09 represent the very top lunar regolith surface, and CE5-D14 and CE5-D15 represent a depth of ∼3 cm (Wu et al., 2022) of the same locations. The result showed that, for CE-5 LMS, the water contents of spectra CE5-D14 and CE5-D15 were obviously lower than that of spectra CE5-D04 and CE5-D09, supporting this mechanism.

4.2. Plume-Regolith Interactions at the CE-5 and CE-6 Landing Sites

As shown by the PCAM images (Figures 1a and 1c), the CE-6 landing site is relatively flatter and smoother than CE-5. Several meter-sized rocks are distributed in the CE-5 region, including "Shi Gandang" (about 0.5 m in size), while there are no apparent boulders in the CE-6 region. This indicates that the CE-6 site is more uniform, and indeed the observed water content variations of CE-6 (101 ppm) are smaller than those of CE-5 (131 ppm). The significant difference in water content between "Shi Gandang" (131 ppm) and the surrounding regolith (0–1 ppm) might be due to their distinct formation mechanisms. Two possible explanations were proposed. The first was that the water observed in "Shi Gandang" might be endogenous (H. Lin et al., 2022). The second suggested that the top surface of regolith with a higher water content was blown by the engine plume to the rock surface (Liu et al., 2022). Both models have their drawbacks. A water abundance of <10 ppm was reported for the returned CE-5 basalts (Hu et al., 2021) similar to former measurements of Apollo basalts (Greenwood et al., 2010), which are highly likely to be the same as the local half-meter "Shi Gandang" (Qian, Xiao, Head, et al., 2021) rock. Such a dry bulk basalt cannot explain the abundant water content of Shi Gandang (131 ppm), and even if they exist, they would be lost during 2.8 Ga years of gardening (Cui et al., 2024). In addition, based on our results and all previous work (H. Lin et al., 2022; Liu et al., 2022), the water content of the lunar regolith (0–1 ppm) is much lower than ∼131 ppm, arguing against the hypothesis that the abnormally high water content of Shi Gandang is from a thin covering of lunar regolith; furthermore, such a regolith coverage is not observed in the PCAM data (Figure 1a).

As an alternative to these two hypotheses for the high water content of Shi Gandang, we propose another possible mechanism. The engine exhaust of the CE-5 lander is capable of injecting a portion of the water plume into the surface voids of "Shi Gandang" due to its high porosity. We hypothesize that this part of plume-emplaced water was then gradually released (Figure 6) to the rock surface, similar to the lunar regolith, as we model below. An example supporting this mechanism is the CE-6 D22 observation characterized by the highest water content of lunar regolith, and showing obvious shadows (Figure 3b). We hypothesize that less water was lost after being injected into the lunar regolith because of the relatively low temperature shielded by shadows, which results in a higher water content.

To better understand the contribution of the engine exhaust plume to surface water migration, as discussed above, we developed a numerical model. In our modeling, we consider only water molecules, as they are dominant in the molar fraction, with higher adsorption energy on lunar minerals than CO_2 and N_2 (Sarantos & Tsavachidis, 2021). The water adsorption and migration process were divided into two stages: (a) Vapor Input Stage (Figure 6a-Left): The lander's plume establishes ambient conditions (Zhang et al., 2022) with vapor pressure >20 Pa and duration >10s, during which water vapor diffuses into regolith and adsorbs onto grain surface; (b) Vapor Release Stage (Figure 6a-Right): After the engine was turned off, the ambient vapor would quickly disappear and the absorbed water molecules would escape in space. The water content of a very shallow regolith layer (∼26 μm thick; Chuanjiao Zhou et al., 2022) is modeled since the penetration depth of the visible near-infrared spectrometer is in microns (Lv et al., 2018). The water content at different depths was weight-averaged following the Lambert-Berg law (Chuanjiao Zhou et al., 2022; Lv et al., 2018) for better comparison with spectral data.

In the vertical direction, only a one-dimensional numerical model was considered. This was because, in the horizontal direction, the plume-influenced distance could obviously be orders of magnitude larger than the vapor penetration depth. Governing equations, boundary conditions, and numerical tools are introduced in Section 2. Surface temperature variation and background water molecule density at the landing site were used to constrain the simulation based on Diviner and M^3 data. Most of the key parameters of the regolith at the CE-6 landing site have previously been reported (C. Li et al., 2024), and the values we adopted are documented in Table 2. However, both the adsorption energy and effective regolith pore size for Knudsen diffusion remain highly uncertain. Therefore, data from Apollo samples (highland: 72501 and 14163; mare: 10084 and 12001) (Jones et al., 2020; Poston et al., 2015; Schörghofer, 2023) were used. The water adsorption energy was considered in the range of 0.6–1.2 eV, and the effective pore size was also considered in the range from 5.41 to 38.98 μm (C. Li et al., 2024). We further constrained the range of water adsorption energy to 0.9–1.2 eV, and the theoretical basis can be found in the description within the "Constraining Model Parameters Using Remote Sensing Observations" section.

We conducted 100 numerical simulations (gray curves in Figure 6b), with adsorption energy and regolith pore size randomly generated within reasonable intervals using the Monte Carlo method. Plume pressure was set at 20 Pa, and landing duration was set at 10 s. Vapor pressure higher than 20 Pa and plume duration longer than 10 s

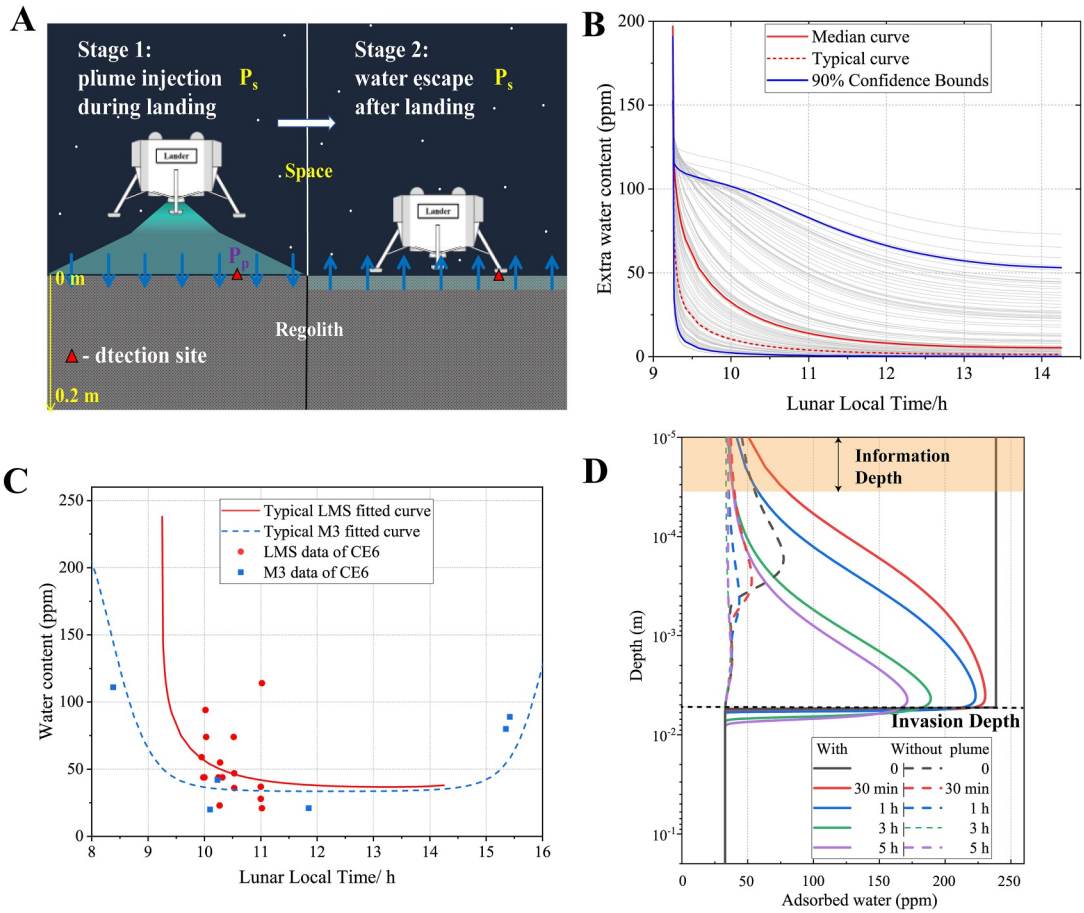

Figure 6. Key simulation results of the water injection and release model. (a) Schematic diagram of the effect of rocket exhaust plume on the water content of shallow lunar regolith. (b) Results of extra water content (additional water content to the case without plume) after plume injection, with adsorption energy and pore size values selected by the Monte Carlo method. The red solid curve is the one in the middle of all the curves, with the adsorption energy of 1.04 eV and pore size of 26.14 μm. The typical case corresponds to an adsorption energy of 1.01 eV and pore size of 20.00 μm. (c) Comparison of the results of typical case (red dashed line in c) with and without plume affecting water content change. (d) Vertical water content profile at different times for a typical case with adsorption energy of 1.01 eV and pore size of 20.00 μm after 10s explosion under 20 Pa water vapor. Note that the depth is in log scale and the shadowed region is the depth that can be detected by spectra.

would not affect the water content measurement due to the shallow measurement depth. In all realizations, the plume-induced water content is comparable to or even larger than the reference content. The median curve is close to the case of adsorption energy 1.04 eV and pore size of 26.14 μm. For an adsorption energy of 1.01 eV and pore size of 20.00 μm, the mean squared error between the total water content curve and CE-6 data points is minimized, which represents a typical case (also demonstrated in Figure 6b. Compared to CE-6 LMS data and M^3 data, the simulation result was in good agreement with the observed data, as shown in Figure 6c).

Figure 6d shows the vertical water content profile evolution after landing (with) in the typical numerical simulation (adsorption energy 1.01 eV, pore size 20.00 μm). At the moment that the engine was turned off, the water could be injected into ~5.3 mm depth, which is much deeper than the penetration depth of LMS. When the injected water started to vaporize, it would be released from the topmost layer, making the water content near the surface decrease rapidly. Meanwhile, the internal water could supply the shallow detectable region. As a result, the detected water content, although monotonically decreased before noon, would still be significantly higher than the baseline (fitted with M^3 data) in several lunar hours.

These simulation results effectively support our hypothesis based on LMS observations: the engine plume can induce long-term residual water content into shallow regolith at CE-5/6 landing sites, which may lead to sample contamination and potential misinterpretation of volatile content.

5. Conclusions

Based on both LMS observations and water injection-diffusion modeling, we propose that rocket exhaust produces surface water migration at lunar landing sites at least on a lunar day. This mechanism must be considered and mitigated in future interpretation of lunar surface water data if obtained next to the lunar lander. The injected water from the descent rocket plume would be even more prominent in lunar polar regions, where the highest temperature is much lower than in middle and low latitude regions (Williams et al., 2017), and therefore diffusion would proceed much more slowly. In our modeling of potential rocket plume-lunar regolith interactions at the upcoming China's Chang'e-7 landing site in the lunar south pole (Chi Wang et al., 2024), we found that at the Chang'e-7 (CE-7) landing site, the temperature varies between 40K and 216K, which is much lower than that of the CE-5/6 landing sites. Therefore, plume-induced water would not only be adsorbed but also directly condense into ice. Assuming 10 s emplacement under 20 Pa water vapor, the condensed ice could last for hundreds of years, even at an overestimated temperature of 216K. In lower temperature cases, such as the CE-7 landing site, the descent engine rocket plume exhaust might result in a permanent contamination with lunar surface water signatures; therefore, it must be taken into account in future polar exploration from a planetary protection perspective (Estacio et al., 2024; Estacio et al., 2024; Prem et al., 2025; Prem et al., 2025).

Conflict of Interest

The authors declare no conflicts of interest relevant to this study.

Availability Statement

The CE-5 and CE-6 LMS and LCAM data sets were downloaded from the Lunar and Planetary Data Release System, the Ground Research and Application System of China's Lunar and Planetary Exploration Program, China National Space Administration, 2020 (https://moon.bao.ac.cn/ce5web/moonGisMap.search). We also uploaded them to the supplementary materials. The M^3 Level 2 reflectance data are available from the PDS Image Node (https://planetarydata.jpl.nasa.gov/img/data/m3/CH1M3_0004/DATA/) (Malaret et al., 2011). The LROC NAC data were downloaded from the Planetary Data System Geoscience Node (https://pds.lroc.im-ldi.com/data/LRO-L-LROC-3-CDR-V1.0/) (Robinson, 2009). Diviner GCP data were also downloaded from PDS Geoscience Node (https://pds-geosciences.wustl.edu/lro/urn-nasa-pds-lro_diviner_derived1/data_derived_gcp/) (Paige, 2018).

Acknowledgments
The authors thank the China National Space Administration for providing the Chang'e-5 and Chang'e-6 scientific data. The authors thank Prof. Xin Ren and Prof. Bin Liu for discussing the Chang'e-5 and Chang'e-6 LMS data processing and analyzing. This work was funded by the HK RGC Grants 17307025, JLFS/P-702/24 and HKU Internal Grants for Member of the Chinese Academy of Sciences (102009906, 102010100, 2401102769). Y. Y. and K. X. were funded by the National Key Research and Development Program of China (2021YFA0717200).

References

Anand, M., Tartèse, R., & Barnes, J. J. (2014). Understanding the origin and evolution of water in the Moon through lunar sample studies. *Philosophical Transactions of the Royal Society A: Mathematical, Physical and Engineering Sciences*, *372*(2024), 20130254. https://doi.org/10.1098/rsta.2013.0254

Clark, R. N., Pieters, C. M., Green, R. O., Boardman, J. W., & Petro, N. E. (2011). Thermal removal from near-infrared imaging spectroscopy data of the Moon. *Journal of Geophysical Research*, *116*, E00G16. https://doi.org/10.1029/2010JE003751

Clegg, R. N., Jolliff, B. L., Robinson, M. S., Hapke, B. W., & Plescia, J. B. (2014). Effects of rocket exhaust on lunar soil reflectance properties. *Icarus*, *227*, 176–194. https://doi.org/10.1016/j.icarus.2013.09.013

Clegg-Watkins, R. N., Jolliff, B. L., Boyd, A., Robinson, M. S., Wagner, R., Stopar, J. D., et al. (2016). Photometric characterization of the Chang'e-3 landing site using LROC NAC images. *Icarus*, *273*, 84–95. https://doi.org/10.1016/j.icarus.2015.12.010

Clendenen, A. R., Aleksandrov, A., Jones, B. M., Loutzenhiser, P. G., Britt, D. T., & Orlando, T. M. (2022). Temperature programmed desorption comparison of lunar regolith to lunar regolith simulants LMS-1 and LHS-1. *Earth and Planetary Science Letters*, *592*, 117632. https://doi.org/10.1016/j.epsl.2022.117632

Colaprete, A., Schultz, P., Heldmann, J., Wooden, D., Shirley, M., Ennico, K., et al. (2010). Detection of water in the LCROSS ejecta plume. *Science*, *330*(6003), 463–468. https://doi.org/10.1126/science.1186986

Cui, Z., Yang, Q., Zhang, Y.-Q., Wang, C., Xian, H., Chen, Z., et al. (2024). A sample of the Moon's far side retrieved by Chang'e-6 contains 2.83-billion-year-old basalt. *Science*, *386*(6728), 1395–1399. https://doi.org/10.1126/science.adt1093

Estacio, B., Hurley, D., Prem, P., & Vondrak, R. (2024). Simulations of rocket exhaust propagation on the Moon. *Presented at the AAS/division for planetary sciences meeting abstracts* (Vol. 56, p. 413).

Fisher, E. A., Lucey, P. G., Lemelin, M., Greenhagen, B. T., Siegler, M. A., Mazarico, E., et al. (2017). Evidence for surface water ice in the lunar polar regions using reflectance measurements from the Lunar Orbiter Laser Altimeter and temperature measurements from the Diviner Lunar Radiometer Experiment. *Icarus*, *292*, 74–85. https://doi.org/10.1016/j.icarus.2017.03.023

Gaddis, L. R., Joy, K. H., Bussey, B. J., Carpenter, J. D., Crawford, I. A., Elphic, R. C., et al. (2023). Recent exploration of the Moon: Science from lunar missions since 2006. *Reviews in Mineralogy and Geochemistry*, *89*(1), 1–51. https://doi.org/10.2138/rmg.2023.89.01

Gladstone, G. R., Retherford, K. D., Egan, A. F., Kaufmann, D. E., Miles, P. F., Parker, J. W., et al. (2012). Far-ultraviolet reflectance properties of the Moon's permanently shadowed regions. *Journal of Geophysical Research*, *117*(E12), 2011JE003913. https://doi.org/10.1029/2011JE003913

Greenwood, J., Itoh, S., Sakamoto, N., Taylor, L., Warren, P., & Yurimoto, H. (2010). Water in Apollo rock samples and the D/H of lunar apatite. *Presented at the 41st annual lunar and planetary science conference* (p. 2439).

Groussin, O., A'Hearn, M. F., Li, J.-Y., Thomas, P. C., Sunshine, J. M., Lisse, C. M., et al. (2007). Surface temperature of the nucleus of Comet 9P/Tempel 1. *Icarus*, *187*(1), 16–25. https://doi.org/10.1016/j.icarus.2006.08.030

Gueymard, C. A. (2004). The Sun's total and spectral irradiance for solar energy applications and solar radiation models. *Solar Energy*, *76*(4), 423–453. https://doi.org/10.1016/j.solener.2003.08.039

Gunn, R. D., & King, C. J. (1969). Mass transport in porous materials under combined gradients of composition and pressure. *AIChE Journal*, *15*(4), 507–514. https://doi.org/10.1002/aic.690150409

Hayne, P. O., Hendrix, A., Sefton-Nash, E., Siegler, M. A., Lucey, P. G., Retherford, K. D., et al. (2015). Evidence for exposed water ice in the Moon's south polar regions from Lunar Reconnaissance Orbiter ultraviolet albedo and temperature measurements. *Icarus*, *255*, 58–69. https://doi.org/10.1016/j.icarus.2015.03.032

He, W., Lv, W., & Dickerson, J. (2014). *Gas transport in solid oxide fuel cells*. Springer.

Head, J. W., Wilson, L., Deutsch, A. N., Rutherford, M. J., & Saal, A. E. (2020). Volcanically induced transient atmospheres on the Moon: Assessment of duration, significance, and contributions to polar volatile traps. *Geophysical Research Letters*, *47*(18), e2020GL089509. https://doi.org/10.1029/2020GL089509

Honniball, C. I., Lucey, P. G., Ferrari-Wong, C. M., Flom, A., Li, S., Kaluna, H. M., & Takir, D. (2020). Telescopic observations of lunar hydration: Variations and abundance. *Journal of Geophysical Research: Planets*, *125*(9), e2020JE006484. https://doi.org/10.1029/2020JE006484

Hu, S., He, H., Ji, J., Lin, Y., Hui, H., Anand, M., et al. (2021). A dry lunar mantle reservoir for young mare basalts of Chang'e-5. *Nature*, *600*(7887), 49–53. https://doi.org/10.1038/s41586-021-04107-9

Hurley, D. M., Siegler, M. A., Cahill, J. T., Colaprete, A., Costello, E., Deutsch, A. N., et al. (2023). Surface volatiles on the Moon. *Reviews in Mineralogy and Geochemistry*, *89*(1), 787–827. https://doi.org/10.2138/rmg.2023.89.18

Jia, B., Fa, W., Xie, M., Tai, Y., & Liu, X. (2021). Regolith properties in the Chang'e-5 landing region of the Moon: Results from multi-source remote sensing observations. *Journal of Geophysical Research: Planets*, *126*(7), e2021JE006934. https://doi.org/10.1029/2021JE006934

Jin, S., Hao, M., Guo, Z., Yin, B., Ma, Y., Deng, L., et al. (2024). Evidence of a hydrated mineral enriched in water and ammonium molecules in the Chang'e-5 lunar sample. *Nature Astronomy*, *8*(9), 1127–1137. https://doi.org/10.1038/s41550-024-02306-8

Jones, B. M., Aleksandrov, A., Dyar, M. D., Hibbitts, C. A., & Orlando, T. M. (2020). Investigation of water interactions with Apollo lunar regolith grains. *Journal of Geophysical Research: Planets*, *125*(6), e2019JE006147. https://doi.org/10.1029/2019JE006147

Jones, B. M., Aleksandrov, A., Hibbitts, K., Dyar, M. D., & Orlando, T. M. (2018). Solar wind-induced water cycle on the Moon. *Geophysical Research Letters*, *45*(20). https://doi.org/10.1029/2018GL080008

Keihm, S. J. (1984). Interpretation of the lunar microwave brightness temperature spectrum: Feasibility of orbital heat flow mapping. *Icarus*, *60*(3), 568–589. https://doi.org/10.1016/0019-1035(84)90165-9

Kulchitsky, A. V., Hurley, D. M., Johnson, J. B., Duvoy, P. X., & Zimmerman, M. (2018). Solar wind access to grains in the upper layer of regolith. *Journal of Geophysical Research: Planets*, *123*(4), 972–981. https://doi.org/10.1002/2017je005392

Li, C., Hu, H., Yang, M.-F., Liu, J., Zhou, Q., Ren, X., et al. (2024). Nature of the lunar far-side samples returned by the Chang'e-6 mission. *National Science Review*, *11*(11), nwae328. https://doi.org/10.1093/nsr/nwae328

Li, C., Hu, H., Yang, M.-F., Pei, Z.-Y., Zhou, Q., Ren, X., et al. (2022). Characteristics of the lunar samples returned by the Chang'e-5 mission. *National Science Review*, *9*(2), nwab188. https://doi.org/10.1093/nsr/nwab188

Li, S., & Li, L. (2011). Radiative transfer modeling for quantifying lunar surface minerals, particle size, and submicroscopic metallic Fe. *Journal of Geophysical Research*, *116*(E9), 2011JE003837. https://doi.org/10.1029/2011JE003837

Li, S., Lucey, P. G., Milliken, R. E., Hayne, P. O., Fisher, E., Williams, J.-P., et al. (2018). Direct evidence of surface exposed water ice in the lunar polar regions. *Proceedings of the National Academy of Sciences*, *115*(36), 8907–8912. https://doi.org/10.1073/pnas.1802345115

Li, S., & Milliken, R. E. (2016). An empirical thermal correction model for Moon Mineralogy Mapper data constrained by laboratory spectra and Diviner temperatures. *Journal of Geophysical Research: Planets*, *121*(10), 2081–2107. https://doi.org/10.1002/2016JE005035

Lin, H., Li, S., Xu, R., Liu, Y., Wu, X., Yang, W., et al. (2022). In situ detection of water on the Moon by the Chang'e-5 lander. *Science Advances*.

Lin, J., Xian, H., Yang, Y., Li, S., Xi, J., Lin, X., et al. (2025). Differences in space weathering between the near and far side of the Moon: Evidence from Chang'e-6 samples. *National Science Review*, *12*(6), nwaf087. https://doi.org/10.1093/nsr/nwaf087

Liu, J., Liu, B., Ren, X., Li, C., Shu, R., Guo, L., et al. (2022). Evidence of water on the lunar surface from Chang'e-5 in-situ spectra and returned samples. *Nature Communications*, *13*(1), 3119. https://doi.org/10.1038/s41467-022-30807-5

Lu, X., Chen, J., Cao, H., Liu, C., Jia, Z., Yin, C., et al. (2025). Space weathering properties of Chang'e-6 soils and implication for regolith evolution of young lunar maria. *The Astrophysical Journal Letters*, *983*(1), L1. https://doi.org/10.3847/2041-8213/adbffc

Lu, Y., Wang, W., Jiao, H., Xu, T., Chen, X., & Wu, Y. (2024). Lunar south polar water cycle and water resources: Diurnal and spatial variations in surficial hydration from repeated Moon mineralogy mapper observations. *Geophysical Research Letters*, *51*(7), e2023GL107499. https://doi.org/10.1029/2023GL107499

Lv, S., Zeng, Y., Wen, J., Zhao, H., & Su, Z. (2018). Estimation of penetration depth from soil effective temperature in microwave radiometry. *Remote Sensing*, *10*(4), 519. https://doi.org/10.3390/rs10040519

Malaret, E., Guasqui, P., McLaughlin, S., Sunshine, J., Besse, S., Clark, R., & Isaacson, P. (2011). CH1-ORB Moon M3 4 L2 reflectance Near-IR spectral images V1.0, CH1-ORB-L-M3-4-L2-reflectance-V1.0. *Dataset] NASA Planetary Data System*. https://doi.org/10.17189/1520414

McCubbin, F. M., Barnes, J. J., Ni, P., Hui, H., Klima, R. L., Burney, D., et al. (2023). Endogenous lunar volatiles. *Reviews in Mineralogy and Geochemistry*, *89*(1), 729–786. https://doi.org/10.2138/rmg.2023.89.17

Milliken, R. E., & Li, S. (2017). Remote detection of widespread indigenous water in lunar pyroclastic deposits. *Nature Geoscience*, *10*(8), 561–565. https://doi.org/10.1038/ngeo2993

Paige, D. (2018). LRO DLRE level 5 PRP V2.0 [Dataset]. *NASA Planetary Data System, LRO-L-DLRE-5-PRP-V2.0*. https://doi.org/10.17189/1520650

Pieters, C. M., Goswami, J. N., Clark, R. N., Annadurai, M., Boardman, J., Buratti, B., et al. (2009). Character and spatial distribution of OH/H_2O on the surface of the Moon seen by M^3 on Chandrayaan-1. *Science*, *326*(5952), 568–572. https://doi.org/10.1126/science.1178658

Poston, M. J., Grieves, G. A., Aleksandrov, A. B., Hibbitts, C. A., Dyar, M. D., & Orlando, T. M. (2015). Temperature programmed desorption studies of water interactions with Apollo lunar samples 12001 and 72501. *Icarus*, *255*, 24–29. https://doi.org/10.1016/j.icarus.2014.09.049

Prem, P., Honniball, C., Farrell, W., Mandt, K., & Gawronska, A. (2025). Understanding the impact of exploration on the lunar volatile system. *LPI Contribution*, *3090*, 1632.
Qian, Y., Head, J., Michalski, J., Wang, X., Van Der Bogert, C. H., Hiesinger, H., et al. (2024). Long-lasting farside volcanism in the Apollo basin: Chang'e-6 landing site. *Earth and Planetary Science Letters*, *637*, 118737. https://doi.org/10.1016/j.epsl.2024.118737
Qian, Y., Xiao, L., Head, J. W., Wöhler, C., Bugiolacchi, R., Wilhelm, T., et al. (2021). Copernican-aged (<200 ma) impact ejecta at the Chang'e-5 landing site: Statistical evidence from crater morphology, morphometry, and degradation models. *Geophysical Research Letters*, *48*(20), e2021GL095341. https://doi.org/10.1029/2021GL095341
Qian, Y., Xiao, L., Wang, Q., Head, J. W., Yang, R., Kang, Y., et al. (2021). China's Chang'e-5 landing site: Geology, stratigraphy, and provenance of materials. *Earth and Planetary Science Letters*, *561*, 116855. https://doi.org/10.1016/j.epsl.2021.116855
Qian, Y., Xiao, L., Zhao, J., Head, J. W., He, Q., Xu, H., et al. (2024). First magnetic and spectroscopic constraints on attenuated space weathering at the Chang'e-5 landing site. *Icarus*, *410*, 115892. https://doi.org/10.1016/j.icarus.2023.115892
Qiao, L., Hess, M., Xu, L., Wöhler, C., Head, J. W., Chen, J., et al. (2023). Extensive lunar surface disturbance at the Chang'e-5 mission landing site: Implications for future lunar base design and construction. *Journal of Geophysical Research: Planets*, *128*(6), e2022JE007730. https://doi.org/10.1029/2022JE007730
Reinecke, S. A., & Sleep, B. E. (2002). Knudsen diffusion, gas permeability, and water content in an unconsolidated porous medium. *Water Resources Research*, *38*(12). https://doi.org/10.1029/2002WR001278
Ren, X., Guo, L., Yu, S., Liu, B., Liu, D., Liu, J., et al. (2024). Chang'e-5 in situ spectra revealing meter-scale surface temperature distribution characteristic of the Moon. *The Astronomical Journal*, *168*(3), 105. https://doi.org/10.3847/1538-3881/ad566f
Robinson, M. (2009). LRO Moon LROC 3 CDR V1.0, LRO-L-LROC-3-CDR-V1.0 [Dataset]. *NASA Planetary Data System*. https://doi.org/10.17189/1520241
Robinson, M. S., Brylow, S. M., Tschimmel, M., Humm, D., Lawrence, S. J., Thomas, P. C., et al. (2010). Lunar Reconnaissance Orbiter Camera (LROC) instrument overview. *Space Science Reviews*, *150*(1–4), 81–124. https://doi.org/10.1007/s11214-010-9634-2
Saal, A. E., Hauri, E. H., Cascio, M. L., Van Orman, J. A., Rutherford, M. C., & Cooper, R. F. (2008). Volatile content of lunar volcanic glasses and the presence of water in the Moon's interior. *Nature*, *454*(7201), 192–195. https://doi.org/10.1038/nature07047
Sarantos, M., & Tsavachidis, S. (2021). Lags in desorption of lunar volatiles. *The Astrophysical Journal Letters*, *919*(2), L14. https://doi.org/10.3847/2041-8213/ac205b
Schörghofer, N. (2023). Adsorption kinetics of water and argon on lunar grains. *The Planetary Science Journal*, *4*(9), 164. https://doi.org/10.3847/PSJ/acf19b
Swenson, H., & Stadie, N. P. (2019). Langmuir's theory of adsorption: A Centennial review. *Langmuir*, *35*(16), 5409–5426. https://doi.org/10.1021/acs.langmuir.9b00154
Tjaden, B., Cooper, S. J., Brett, D. J., Kramer, D., & Shearing, P. R. (2016). On the origin and application of the Bruggeman correlation for analysing transport phenomena in electrochemical systems. *Current Opinion in Chemical Engineering*, *12*, 44–51. https://doi.org/10.1016/j.coche.2016.02.006
Wang, C., Jia, Y., Xue, C., Lin, Y., Liu, J., Fu, X., et al. (2024). Scientific objectives and payload configuration of the Chang'e-7 mission. *National Science Review*, *11*(2), nwad329. https://doi.org/10.1093/nsr/nwad329
Wang, C., Sanlang, S., Tong, X., Xu, X., Feng, Y., & Li, Z. (2023). Exploring the effects of the rocket exhaust of the Chang'e-5 lander on the lunar regolith using LROC NAC and landing camera images. *Icarus*, *403*, 115649. https://doi.org/10.1016/j.icarus.2023.115649
Wang, Y., Xie, H., Wang, C., Tong, X., Liu, S., & Xu, X. (2023). Determination of the spatial extent of the engine exhaust-disturbed region of the Chang'e-4 landing site using LROC NAC images. *Ieee Journal of Selected Topics in Applied Earth Observations and Remote Sensing*, *16*, 468–481. https://doi.org/10.1109/jstars.2022.3227364
Williams, J.-P., Paige, D. A., Greenhagen, B. T., & Sefton-Nash, E. (2017). The global surface temperatures of the Moon as measured by the Diviner Lunar Radiometer Experiment. *Icarus*, *283*, 300–325. https://doi.org/10.1016/j.icarus.2016.08.012
Wu, X., Liu, Y., Yang, Y., Guo, D., Du, J., Li, S., et al. (2022). Mineralogy and regolith maturity at the Chang'e-5 landing site inferred from the Lunar Mineralogical Spectrometer. *Earth and Planetary Science Letters*, *594*, 117747. https://doi.org/10.1016/j.epsl.2022.117747
Xiao, X., Yu, S., Huang, J., Zhang, H., Zhang, Y., & Xiao, L. (2022). Thermophysical properties of the regolith on the lunar far side revealed by the in situ temperature probing of the Chang'e-4 mission. *National Science Review*, *9*(11), nwac175. https://doi.org/10.1093/nsr/nwac175
Xu, R., Li, C., Yuan, L., Lv, G., Xu, S., Li, F., et al. (2022). Lunar mineralogical spectrometer on Chang'e-5 mission. *Space Science Reviews*, *218*(5), 41. https://doi.org/10.1007/s11214-022-00910-6
You, J., Zhang, X., Yu, H., Zhang, H., Li, C., Bugiolacchi, R., et al. (2023). Unveiling the mechanics of lunar regolith erosion through analysis of CE-4 and CE-5 landing images and fluid simulation. *Acta Astronautica*, *208*, 343–354. https://doi.org/10.1016/j.actaastro.2023.04.024
Zhang, H., Li, C., You, J., Zhang, X., Wang, Y., Chen, L., et al. (2022). The investigation of plume-regolith interaction and dust dispersal during Chang'e-5 descent stage. *Aerospace*, *9*(7), 358. https://doi.org/10.3390/aerospace9070358
Zheng, W., Hu, G., Wu, Y., Jin, Q., Li, Z., & Feng, L. (2023). Chang'e-4 measurements of lunar surface temperatures: Thermal conductivity of the near surface regolith. *IEEE Transactions on Geoscience and Remote Sensing*, *61*, 1–14. https://doi.org/10.1109/TGRS.2023.3245191
Zhou, C., Jia, Y., Liu, J., Li, H., Fan, Y., Zhang, Z., et al. (2022). Scientific objectives and payloads of the lunar sample return mission—Chang'e-5. *Advances in Space Research*, *69*(1), 823–836. https://doi.org/10.1016/j.asr.2021.09.001
Zhou, C., Mo, B., Tang, H., Gu, Y., Li, X., Zhu, D., et al. (2024). Multiple sources of water preserved in impact glasses from Chang'e-5 lunar soil. *Science Advances*, *10*(19), eadl2413. https://doi.org/10.1126/sciadv.adl2413
Zhou, C., Tang, H., Li, X., Zeng, X., Mo, B., Yu, W., et al. (2022). Chang'e-5 samples reveal high water content in lunar minerals. *Nature Communications*, *13*(1), 5336. https://doi.org/10.1038/s41467-022-33095-1